

K. NAPLOCHA<sup>1\*</sup>, J. GRZĘDA<sup>1</sup>, O. TRZASKA<sup>1</sup>, N. RAŻNY<sup>1</sup>, A. DMITRUK<sup>1</sup>

## DEVELOPMENT OF CELLULAR CAST STRUCTURES FOR IMPROVING HEAT TRANSFER IN THERMAL ENERGY STORAGE SYSTEMS

For improving heat transfer in the thermal energy storage system (TES), cast aluminum cellular structures were designed, optimized, and produced by investment casting. The pattern was 3D printed from polylactide (PLA) polymer and then subjected to molding and heat treatment. Selected casting parameters, i.e. temperature of the mold and poured metal, as well as low pressure (vacuum), allowed to production of a complex, thin-walled casting. To evaluate the effectiveness of the structures (enhancers), a lab-scale heat accumulator was constructed and filled with phase change material (PCM) composed of  $\text{KNO}_3$  and  $\text{NaNO}_3$  salts. Thermal cycling, including charging and discharging of the accumulator, was analyzed and compared between systems with pure PCM bed and the one equipped with the produced enhancer. To protect aluminum casting against corrosion with molten salts, nickel plating was applied. Process parameters, such as plating process time and nickel subcoating application time, were determined. Microscopic observations confirmed high-quality, continuous coating on aluminum casting surfaces with characteristic microgrooves remaining after the printed pattern.

*Keywords:* investment casting; cellular structure; PCM heat storage; aluminum alloy; nickel plating

### 1. Introduction

Thermal energy storage systems are being developed to provide high heat capacity utilizing sensible, latent, or thermochemical heat. They use renewable and waste energy to improve the stability and balance between energy supply and demand. Latent thermal energy storage (LTES) is based on phase change materials (PCMs), mainly hydrocarbons, inorganic salts, salt hydrates, stearic acid, and eutectics [1-4]. The PCMs phase transition can take place between the following phases: gas-liquid, solid-solid, solid-gas, and solid-liquid, which, depending on the phases involved in the transformation, may relate, for example, to a change in volume in the system. Systems based on solid-liquid phase change are the most popular solution [5]. PCMs, depending on the phase change temperature, are used in air refrigeration systems (for phase change temperatures up to  $15^\circ\text{C}$ ), in medical, textile, and electronic industries (for temperature ranges from  $15^\circ\text{C}$  to  $90^\circ\text{C}$ ), or cooking and aerospace industry (transition temperatures above  $90^\circ\text{C}$ ) [5,6].

PCMs can accumulate and release large amounts of thermal energy during melting and solidification. Nevertheless, PCMs have low thermal conductivity, which increases the charging and

discharging times of LTES systems. Therefore, several studies have been carried out to enhance heat transfer in the PCM and subsequently improve the working cycle efficiency. Developed in recent years, the phase change composite materials can be produced by incorporating highly conductive particles or fibers, heat pipes (sometimes with fins), or immersing porous metal foams [7-9]. In the case of composites with metallic foams, a decreased temperature gradient in the PCM bed and a sufficient heat transfer are observed. The temperature distribution along the distance from the heat source is improved by 3-4 times [10] in comparison to the pure PCM. Loose particles in PCM, like expandable graphite, can segregate depending on the difference in density, while when compressed, they can reduce the volume of PCM by up to 30-44% by weight [11]. The use of spatial metal structures is of increasing interest due to their high strength-to-density ratio, beneficial thermal conductivity, large surface area, and relatively low cost.

Investigations and analyses, presented by other researchers, most often focused on estimating the increase in heat transfer in the solid-liquid system by the use of porous structures. Due to their continuous architecture containing interconnected elements, a total 3-10-fold increase in heat transfer rate was observed [10].

<sup>1</sup> WROCLAW UNIVERSITY OF SCIENCE AND TECHNOLOGY, FACULTY OF MECHANICAL ENGINEERING, DEPARTMENT OF LIGHTWEIGHT ELEMENTS ENGINEERING, FOUNDRY, AND AUTOMATION, 27 WYBRZEZE WYSPIANSKIEGO STR., 50-370 WROCLAW, POLAND

\* Corresponding author: [krzysztof.naplocha@pwr.edu.pl](mailto:krzysztof.naplocha@pwr.edu.pl)



In the solid state, only the thermal conductivity of metal inserts affects the final heat transfer, but after the melting of PCM also substantial convection improves the process and reduces the charging time. Zhao et al. [10] enhanced convection by introducing the so-called “wind tunnel” and then observed a reduced temperature gradient in the volume occupied by metal foam and overall faster heat transfer in paraffin.

In general, the cellular structures in the PCM bed improve thermal conductivity during both solidification and melting. Metal foam or inserts with smaller cell size, higher volume, or mass can improve heat transfer, although replacing PCM in the storage tank decreases the volumetric heat of fusion. Therefore, additional investigations and more sophisticated solutions are being developed. The copper foam can be supplemented with expandable graphite [12] or, as done by Khalid Lafdi et al. [13], the carbon foam is coated with copper to improve thermomechanical properties. The Cu coating has improved the strength and stiffness of the foam, as well as the rate of heat dissipation and absorption. As a result, the PCM composite becomes a versatile material with significantly reduced weight. Although the

research was limited to a few charging (heating) cycles, copper plating can significantly improve the durability of the porous structure and the process conditions.

The latent heat storage media, as was mentioned at the beginning, are based mainly on the solid-liquid transition. They allow to storage of large amounts of energy in a relatively small volume, which results in one of the lowest costs among known methods of accumulation concepts [14]. High-temperature LTES are promising not only for solar thermal power plants but they are also investigated for industrial waste heat recovery or engine waste heat recovery [15]. An example of the PCM that has been successfully used is an inorganic  $\text{KNO}_3\text{-NaNO}_3$  salt mixture.

In addition to the issue of thermal conductivity, inorganic PCMs have disadvantages such as toxicity, corrosivity, or supercooling [16]. One of the most popular metals for the production of heat exchangers are aluminum alloys [17]. The presence of  $\text{KNO}_3$  and  $\text{NaNO}_3$  salts, both in solid form and in solution, does not affect aluminum. An important factor, however, is the increase in temperature in the presence of nitrates, as a result of

TABLE 1

Thermal properties of typical composite PCM components

Material	CTE ( $10^{-6}$ m/(m K))	Thermal conductivity (W/m K)	Corrosive behavior reactive to
Al	22.2 [27]	237 [27]	<ul style="list-style-type: none"> <li>– pure water – as a result of the reaction with water, a passive layer is formed, slowing down the further process of aluminum surface oxidation [28]</li> <li>– highly acidic (e.g. HCl, HF) or alkaline media (e.g. NaOH, KOH) [18];</li> <li>– chloride ions (responsible for the pitting corrosion of aluminum in pH close to neutral) [18]</li> </ul>
Cu	16.6 [27]	401 [27]	<ul style="list-style-type: none"> <li>– chloride ions [29];</li> <li>– <math>\text{H}_2\text{SO}_4</math> [30];</li> <li>– passivation of metallic copper under oxygen conditions [31]</li> </ul>
Zn	29.7 [27]	116 [27]	<ul style="list-style-type: none"> <li>– passivation of metallic zinc under oxygen conditions [31];</li> <li>– chloride and sulfate ions (increase the solubility of zinc), chromate ions (may form the passive film) [32]</li> </ul>
Graphite	2-6 [27]	90 [27]	<ul style="list-style-type: none"> <li>– acids (<math>\text{HNO}_3</math>, <math>\text{H}_2\text{SO}_4</math>, <math>\text{HClO}_4</math>, <math>\text{H}_2\text{SeO}_4</math>), the products of the reaction are the intercalation compounds [33];</li> <li>– fluorides, fluorine, and bromine [33];</li> <li>– oxygen [34]</li> </ul>
Paraffin	106-480 [27]	0.25 [27]	<ul style="list-style-type: none"> <li>– chlorine [35];</li> <li>– nitrating mixtures, mixture of concentrated <math>\text{HNO}_3</math> and concentrated <math>\text{H}_2\text{SO}_4</math> at elevated temperatures [35];</li> <li>– susceptibility to oxidation at temperatures of 80°C-100°C [35]</li> </ul>
$\text{KNO}_3$	–8.5/243 (II/ $\wedge$ crystal orientation) [27]	0.4-0.5 [27]	<ul style="list-style-type: none"> <li>– susceptibility of <math>\text{NO}_3^-</math> ions to the formation of <math>\text{NO}_2^-</math> ions in elevated temperatures (and thus decreasing the thermal stability of the salt), in the presence of oxygen blanket gas delays the degradation process of <math>\text{NO}_3^-</math> ions and can increase the work of the molten salt [39,40]; the <math>\text{NO}_3^-</math> ions decomposition to <math>\text{NO}_2^-</math> ions in the air begins accordingly for <math>\text{KNO}_3</math>, <math>\text{NaNO}_3</math> and <math>(\text{Na}, \text{K})\text{NO}_3</math> at temperatures: 650°C, 600°C and 295°C; the resulting nitrites of sodium and potassium (<math>\text{KNO}_2</math> and <math>\text{NaNO}_2</math>) lower the melting point of nitrates and may decompose to oxides above temperatures respectively: 410°C and 357°C [41];</li> <li>– <math>\text{NO}_3^-</math> and <math>\text{NO}_2^-</math> ions (and their alkali metal oxides) may react with <math>\text{H}_2\text{O}</math> and <math>\text{CO}_2</math>, and the resulting hydroxides may react with <math>\text{CO}_2</math> forming carbonates (e.g. <math>\text{Na}_2\text{CO}_3</math>), the presence of carbonates elevates the viscosity and may precipitate in the thermal storage system [41];</li> <li>– high pH values and elevated temperatures may indicate the corrosion of containment by molten salts (e.g. the austenitic stainless steels) [40,41]</li> </ul>
$\text{NaNO}_3$	40 (for polycrystalline form, at the room temperature) [36]	0.7-0.9 [37]	
40% $\text{KNO}_3$ : 60% $\text{NaNO}_3$ (solar salt)	54.2-71.4 (30.0-199.2°C Heat/cool range) [37]	0.55 (at 400°C) [38] 0.76 (at 30°C) [37]	

which the pH of the environment may change. In the case of cast aluminum alloys, the presence of alloying additives may affect the susceptibility of the alloy to corrosion. For example, copper particles play a cathodic role in an aluminum alloy and contribute to its susceptibility to corrosion [18-19]. TABLE 1 summarizes the thermal properties of typical composite PCM components. One way to increase corrosion resistance is to cover the surface with an anti-corrosion layer. In the case of applications for heat exchangers, in addition to good anti-corrosion properties, the appropriate thermal conductivity of such a layer is also important. These properties are met by nickel, whose thermal conductivity is  $68.4 \text{ Wm}^{-1}\text{K}^{-1}$  in  $20^\circ\text{C}$  (and approx.  $61.5 \text{ Wm}^{-1}\text{K}^{-1}$  in  $200^\circ\text{C}$ ) [20]. Nickel in the form of a coating can also be enriched with particles increasing its thermal conductivity (e.g. graphene particles, thanks to which the Ni-graphene composite showed a thermal conductivity higher by 15% compared to pure Ni) [20]. Thanks to its thermal properties, nickel can also be used as a filler in PCM composites as a material that improves their thermal conductivity [21]. In addition, nickel shows high ductility [22] and chemical activity (which is used, among others, in catalysts) [23].

The process of electrolytic deposition of nickel layers (nickel plating) is one of the most popular, used on various metals, among others, increasing their resistance to corrosion or electrical conductivity, as well as for decorative and finishing purposes. This process consists of dissolving the positively charged nickel anode under the influence of a direct current (applied to the anode and cathode), the flow of the resulting divalent nickel ions through the electrolyte (nickel salt water solution) towards the negative cathode (coated surface) and reduction of the nickel ions to metallic nickel deposited on the cathode [24]. The authors of [25] manufactured the nickel coat on A356.2 aluminum alloy and its composites with rice husk ash particulates to improve its corrosion resistance. The corrosion tests were carried out in an aerated 3.5% NaCl solution environment. The tests showed an increase in corrosion resistance for A356.2 aluminum alloy and its composites as a result of nickel plating. The nickel electroplating process can also be used to introduce particles into the protective coating to improve the other properties of such coating (e.g.  $\text{TiO}_2$  nanoparticles, thanks to which the increase in hardness and the value of Young's modulus of plated surface were observed) [26].

These briefly described issues have been analyzed and developed in the presented work. The research focused mainly on characterizing the performance of the metal insert, and its ability to increase heat transfer during the charging and discharging cycle. The lightweight hexagonal structure made of the Al-Si alloy was used to fill the laboratory chamber tank filled with the eutectic  $\text{KNO}_3\text{-NaNO}_3$  salt mixture. Measurements of the temperature distribution were performed, gradients at the bed height were determined, as well as the time necessary for complete melting or crystallization of the PCM. Trial tests of covering the inserts with a Ni coating, which is intended to protect the inserts against corrosion in the salt mixture, were carried out.

## 2. Materials and methods

The hexagonal metal structures were produced by the means of a modified investment casting method, including designing of polymer pattern, 3D printing it, molding with a special plaster, heat treatment to burn-out of polymer, and developing desired molding properties (strength, permeability, abrasibility) and finally pouring of liquid aluminum. The Pattern was created in Autodesk Inventor Professional 2018 and next, using the Simplify3D software, transformed into the G-code file. Thin-walled hexagonal patterns were produced from polylactide (PLA) using HBOT 3D printer F300. To create a pattern a wax gating system was attached and then the assembly was placed in the flask for pouring of the molding slurry. After the chemical hardening, the mold was subjected to heat treatment with a maximum temperature of  $730^\circ\text{C}$ . Simultaneously, after the combustion and gasification of the polymer model, a precise cavity adequate to the model's shape was created. For moulding ceramic plaster Randolph Ransom-type R&R® ARGENTUM™ (quartz <50%, cristobalite <50%,  $\text{CaSO}_4$  binder) was used. Preheated mold was put into an autoclave and under the pressure of 0.04 MPa aluminum alloy (AC 44200, Si-10.5%-13.5%; Fe-0.55%; Cu-0.05%; Mn-0.35%; Zn-0.10%; Ti-0.15%; Al-balance) was poured. An exemplary 3D printed model and castings are presented in Fig. 1. The size of the hexagonal cell (14, 18, 20, and 23 mm) and the wall thickness (0.8, 1.0, 1.2, 1.5 mm) were changed during the optimization of geometry. The phase change material (PCM) was composed of  $\text{KNO}_3$  and  $\text{NaNO}_3$  salts provided by Archem, mixed in the proper ratio, and melted together before tests. The weight ratio of the salts was 54:46, to adjust the melting point at  $222^\circ\text{C}$ . For each system, measurements were repeated 4-6 times.

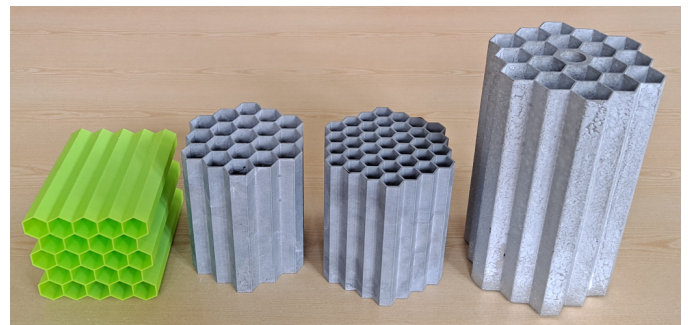


Fig. 1. View of 3D printed PLA model (on the left), the cell size and wall thickness are 18 mm and 0.8 mm (18/0.8), insert castings with geometric parameters, 20/1.0, 14/1.5, 23/1.2, successively from the left, dimensions external: diameter/length approx. 105/120 and 115/180 mm

The constructed laboratory test stand included an insulated cylindrical chamber heated from the bottom flat source. To determine the effectiveness of metal inserts and heat transfer in the PCM chamber, thermocouples were mounted at 11 and 82 mm distance from the heated bottom (Fig. 2). Temperatures were collected and recorded by Adam 4018 type adapter with 8-channels and Visidaq program. Systems with a pure mixture of salts and

the ones with immersed inserts characterized by different wall thicknesses (0.8, 1.0, 1.2 mm) and dimensions of the hexagonal cells (20 and 23 mm) were tested.

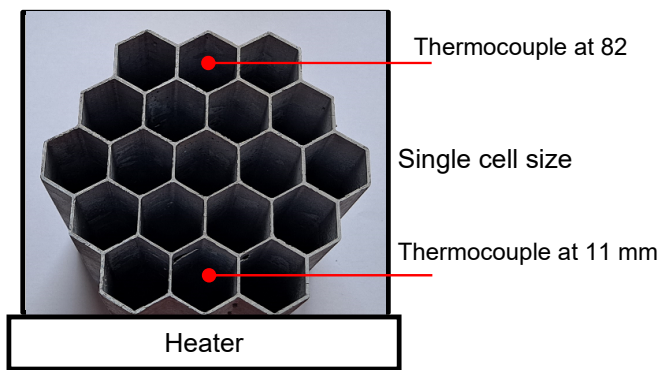


Fig. 2. Scheme of the laboratory heat storage chamber with metal insert and the thermocouples placed in the center of the cells at 11 mm and 82 mm distance from the heated bottom

### 3. Results and discussion

#### 3.1. Thermal performance of aluminum inserts in PCM accumulator

The constructed heat storage unit was charged for 2 h to completely melt the entire PCM. Fig. 3 shows an exemplary temperature measurement for a system without an insert and with the ones type A (single cell size of 23 mm and wall thickness of 1.2 mm, 23/1.2) and B (20/1.0), and the temperature of the heater. The temperature measured far from the heat source (82 mm) shows the efficiency of heat transfer and the reinforcing effect of the insert. After ca. 8 min the heater reaches the temperature of 250°C, sufficient to start the melting of PCM at the bottom. Next, the temperature increases to 270°C and stabilizes for ca. 2 h. This is approximately the time needed for the complete melting of the salt mixture without a metal insert. The slowest temperature increase in the tank occurs for the system with a pure salt mixture without an insert (PCM82). After approx. 3000 s, a slowdown in heating is observed, which proves that energy is absorbed during the transformation of  $\alpha$ - $\beta$  eutectoid transition for salt mixture  $\text{Na}_{0.5}\text{K}_{0.5}\text{NO}_3$  defined in [42] at 110°C. The same phenomenon and deviation in the temperature curve can be noticed for the systems with inserts (A82 and B82), but much earlier, after ca. 1500 s. Following, the temperature increase is uniform until the value corresponding to the phase change of the PCM mixture is reached. The end of the phase transition for the system without an insert, pure PCM, occurs after approx. 6500 s, which is manifested by a temperature jump. A similar phenomenon in the systems with cast inserts takes place 500-1000 s earlier. In general, it can be stated that the fastest complete melting of the bed occurs in the system with insert type A. This is confirmed by a step increase in temperature at about 230°C on thermocouple A82. The temperature of the entire bed is homogeneous, the same at 11 and 82 mm. An important feature of homogenizing

the temperature field leads to a possibly small difference between the lower layers, close to the heater, and the upper ones.

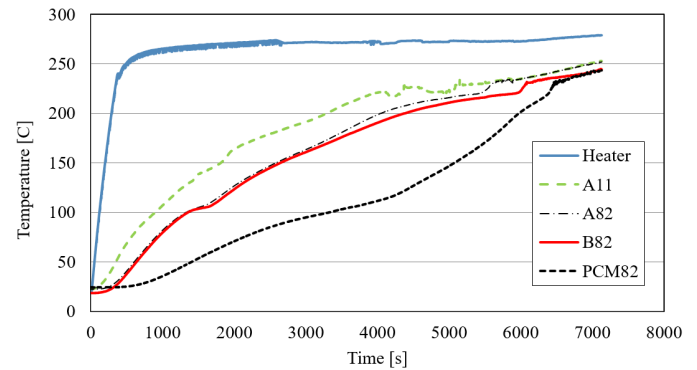


Fig. 3. Temperature profiles during charging measured at the heater and 11 (only A) and 82 mm distances from the bottom for the chamber with pure PCM and PCM with inserts (type A – single cell size of 23 mm and wall thickness of 1.2 mm, 23/1.2 and B – 20/1.0)

In subsequent studies, the temperature gradient in time between the lower and upper thermocouple was calculated. The curves presented in Fig. 4 prove that the highest gradient was shown by the system with pure PCM, it is about 70°C in the time interval of 1000-4500 s. The use of inserts reduces this value more than twice – to 20-30°C. The best thermal performance, slightly better than for the unit with insert type B, characterized the system with the one of type A. The difference in favor of insert type A is 3-4°C.

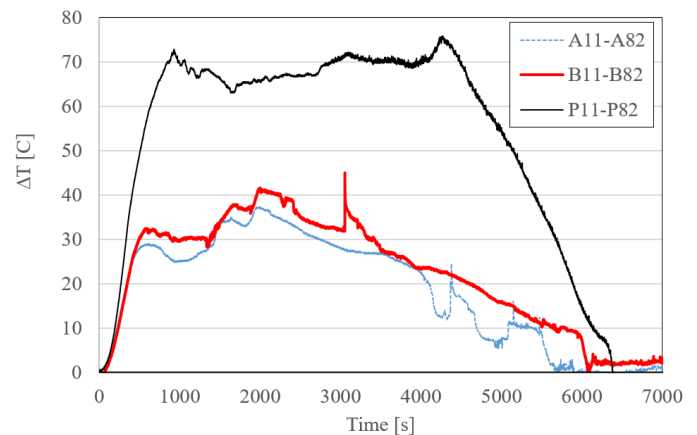


Fig. 4. Temperature gradient between thermocouples at 11 mm and 82 mm from the heated bottom (for the chamber with pure PCM (P11-P82) and composite PCM with inserts type A or B)

The tests performed on one insert allowed to determine the optimal dimensions of the hexagonal structure. In the next step, four inserts were produced with a single cell size of 23 mm, a wall thickness of 1.2 mm, a central cylindrical pipe, and external global dimensions of 115 in diameter and 180 in length. The view of such an insert is shown in Fig. 1 (first on the right). In the produced steel-walled chamber they were mounted in a horizontal position, two at the bottom and two at the top (see Fig. 5). The electric heaters introduced into their central channels were sup-

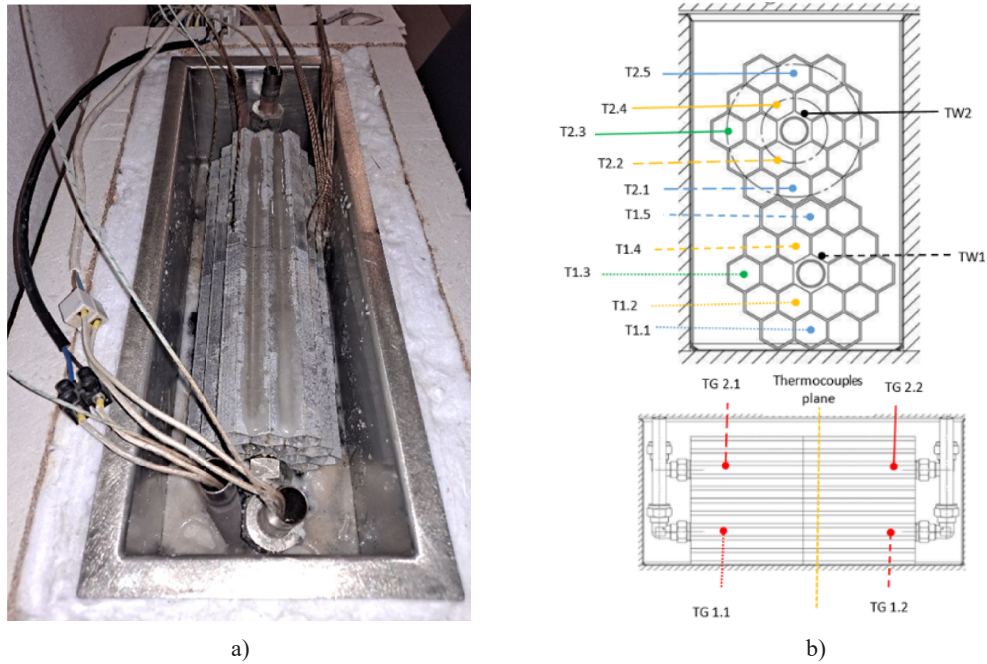


Fig. 5. View of the accumulator chamber (a) and a cross-section with a scheme of the arrangement of thermocouples and their symbols (b)

posed to imitate pipe with heat transfer fluid (HTF) that would be used to charge the accumulator. The scheme of the test stand is shown in the Fig. 5b along with the arrangement and marking of thermocouples. Several heating cycles were performed, maintaining such a power supply to the heaters that the temperatures on the surface (TW1 and TW2) were comparable.

Considering the temperature distribution in the insert cells, values in the upper and lower sections were compared to assess the temperature differences above and below the pipe as well as the effect of convection. The lower outer (T1.1) zone melted at the end, while the side outer (T1.3) behaved slightly better (Fig. 6). The corresponding zones in the upper insert melted about 400 s earlier. It can be stated, that this was due to the

effect of direct heating from the lower section and convection. At a similar time, the outer zone above the lower insert (T1.5), melted. The outer zone above the upper insert (T2.5) heated up approx. 400 s earlier. The difference between the upper, side, and down cells in the lower and upper inserts is similar and amounts to ca. 400 s. However, the difference between the outer zones T1.1 (at the bottom) and T2.5 (at the top) is 800 s, which proves a significant heterogeneity of the temperature field distribution, despite the same ratio and distribution of the metal structure. The temperature distribution close to the heating tube is similar for both inserts T1.2/T2.2 and T1.4/T2.4, regardless of whether it is the upper or lower zone. Melting occurs at the earliest in T1.4 and T2.4 locations, after approx. 600-700 s, i.e. 10-12 minutes.

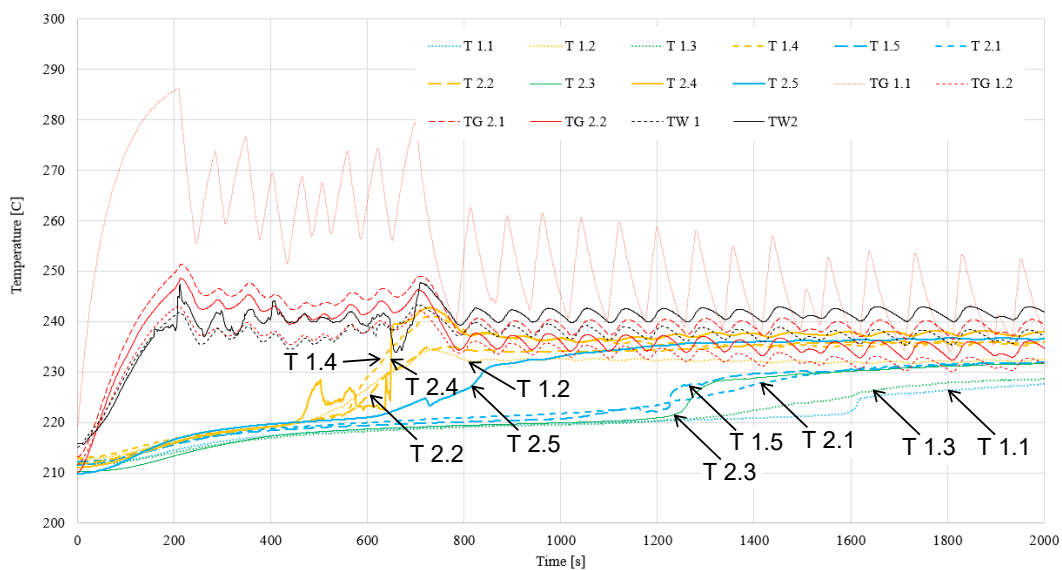


Fig. 6. Temperature profiles measured at the bottom heater and at 5 and 70 mm distances from the bottom for chamber only with PCM and for composite PCM with cast inserts

The simulation carried out in the next step confirms that melting occurs first in these zones. The moment of melting in the upper outer zone T2.5 takes place only about 200 seconds later. It can be concluded that when designing metallic structures, they should be properly modeled to equalize the temperature fields. Summarising, in the lower zones of the PCM, the immersed metal structure should be denser, while the amount of metal should be reduced in the upper zones of the unit.

Preliminary investigations included CFD simulations of the PCM melting process in an open domain with a central heat pipe as an energy source. Transient simulations were conducted with the use of Ansys Fluent software for theoretical models with and without gravity. The lack of gravity forces provide uniform radial thermal energy distribution in all directions, but when gravity is included, the character of energy distribution changes significantly. The buoyancy forces and viscosity start to have a great influence on the flow pattern of the liquid fraction of PCM material (Fig. 7), where the upward flow is dominating. This phenomenon significantly changes heat transfer in the PCM bed, enhancing phase transition in the upper parts of the PCM domain, and restricting heat flow downwards. The general behavior of temperature distribution and liquid fraction interface development coincides with experiment observations and makes initial suggestions on how to equalize energy distribution in PCM bed to reach shorter melting cycles.

### 3.2. Protective Ni galvanic coatings against salt PCM

In the present work, the test samples were cut out from the heat exchanger. Nickel coatings were applied to the inserts using

the COMFORT V galvanic line by Jentner GmbH (Fig. 8). The process of nickel plating of inserts was preceded by electrolytic cleaning with the use of Electrolytic Degreasing Salt JE610 ( $\text{Na}_2\text{SiO}_3$ ,  $\text{NaOH}$ ,  $\text{Na}_2\text{CO}_3$ ). The next stage was electrolytic nickel subcoating with the use of Adhesive Nickel Bath JE303 ( $\text{NiCl}_2$ ,  $\text{HCl}$ ). The nickel coatings were then applied in an electrolytic process using Nickel Bath JE300 ( $\text{NiSO}_4$ ,  $\text{NiCl}_2$ ,  $\text{H}_3\text{BO}_3$ ).

Two types of anodes were used for individual electrolytic processes: steel for electrolytic degreasing and nickel (active) for the production of the nickel subcoating and further nickel plating.

To determine the optimal process parameters, it was proposed to investigate the effect of nickel plating process time and nickel subcoating application time on the quality of the produced nickel coatings. For the procedure, the process of electrolytic degreasing and nickel subcoating was carried out under constant conditions, while the nickel plating time was 5, 10, 20, and 30 min and nickel subcoating time equaled 1, 2, 3, 4, and 5 min. As a reference point, the nickel subcoating application time of 5 min was used together with the time of the proper nickel plating process of 10 min. The current density for both analyzed cases was  $17.5 \text{ A/dm}^2$ .

The individual steps of the process, along with the conditions, were as follows:

- washing samples with distilled water and acetone and drying at  $60^\circ\text{C}$ ,
- electrolytic degreasing (2 min, room temperature, 9V),
- washing with deionized water and drying at  $60^\circ\text{C}$ ,
- electrolytic nickel subcoating (from 1 to 5 min, room temperature, 4 V),
- washing with deionized water and drying at  $60^\circ\text{C}$ ,

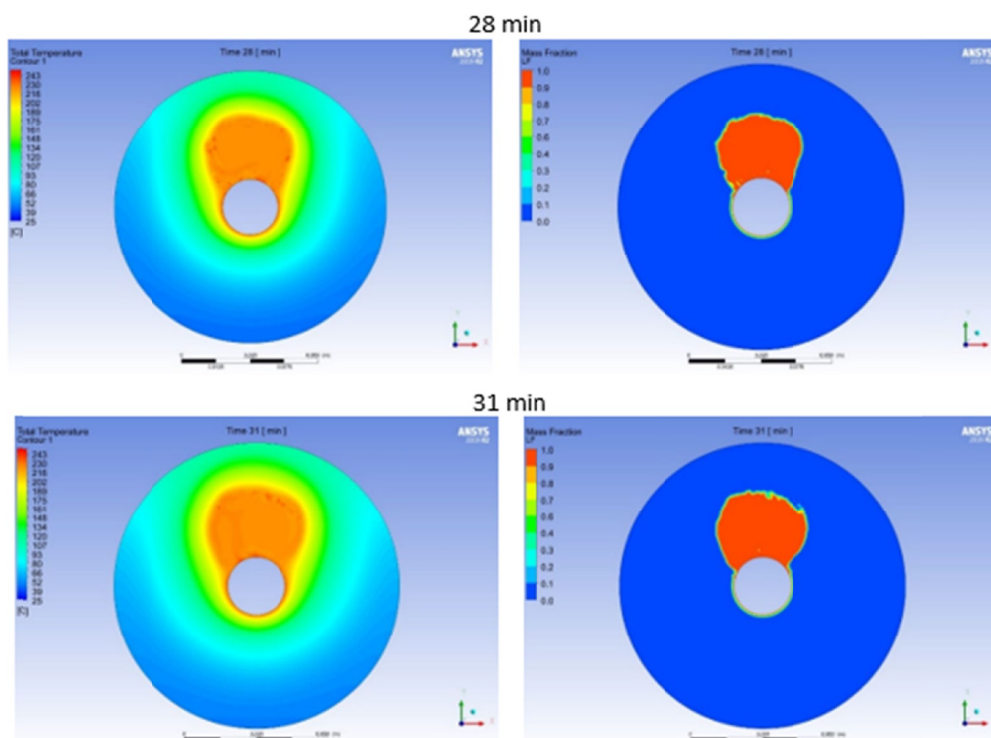
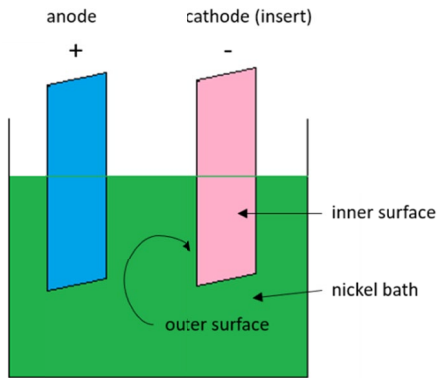


Fig. 7. Maps of the temperature distribution (left) and the liquid fraction area (right) for the time interval of 28-31 min

- nickel plating (60°C, 3V, time: from 5 to 30 min),
- washing with distilled water and drying at 60°C.

The samples were directed to the anode with the outer surface of the insert, marked as “outer”. The surfaces of the inserts that were not facing the anode were marked as “inner” (Fig. 8). The inner surfaces of the samples were analogously the inner surface of the insert, and, respectively, the outer. After each de-greasing and nickel plating step, the samples were weighed to determine the weight of the deposited nickel layer per unit area.

It was found that the optimal time for applying the nickel subcoating was 5 minutes. The reduction of this process duration favored the formation of areas not covered with a nickel layer during the actual nickel plating process (Fig. 9a, Fig. 10a, and b). A difference was also observed between the primary distribution between the outer and inner surfaces of the samples. This is due to the arrangement of the samples to the anode during the process. The nickel coatings of the samples on the surfaces facing directly towards the anode were thicker compared to the



a)   
 Fig. 8. View of the: a) sample marking scheme and b) nickel plating station

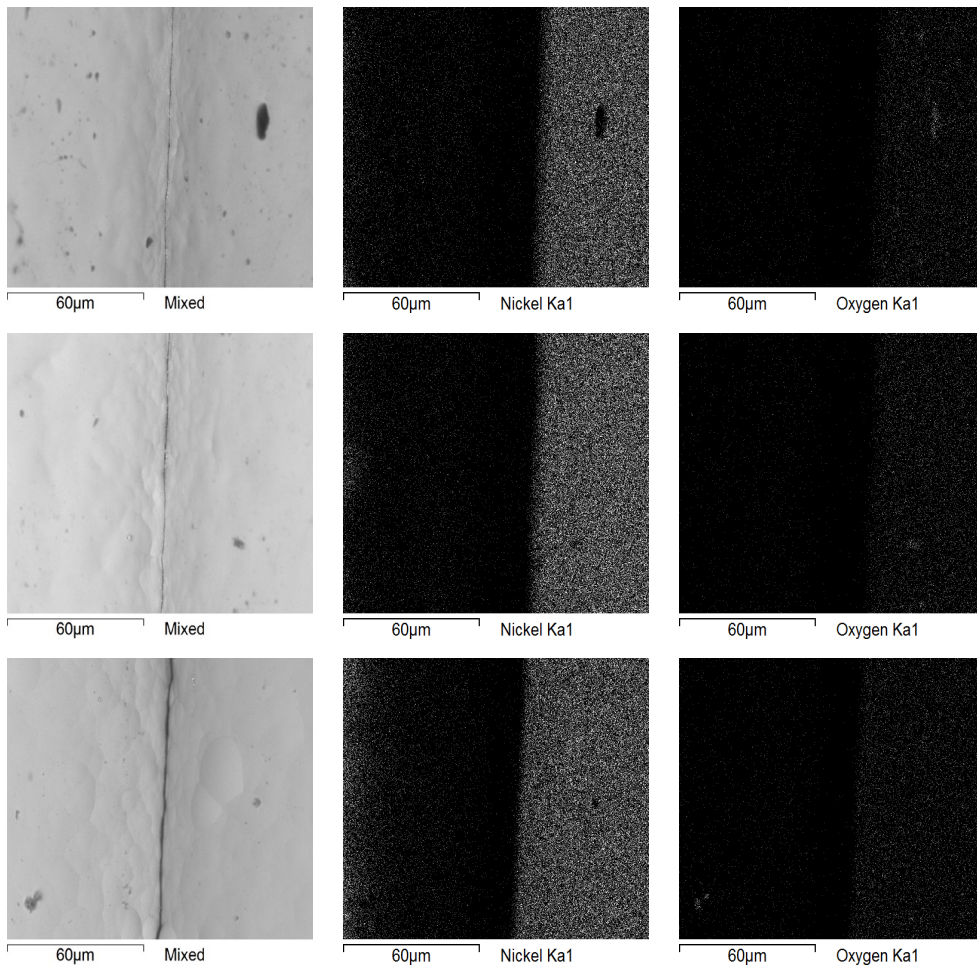


Fig. 9. EDS maps of the distribution of elements in nickel-coated samples’ outer surfaces, for 10 min of nickel plating process and time of sub-coating equalling: a) 1 min, b) 4 min, c) 5 min

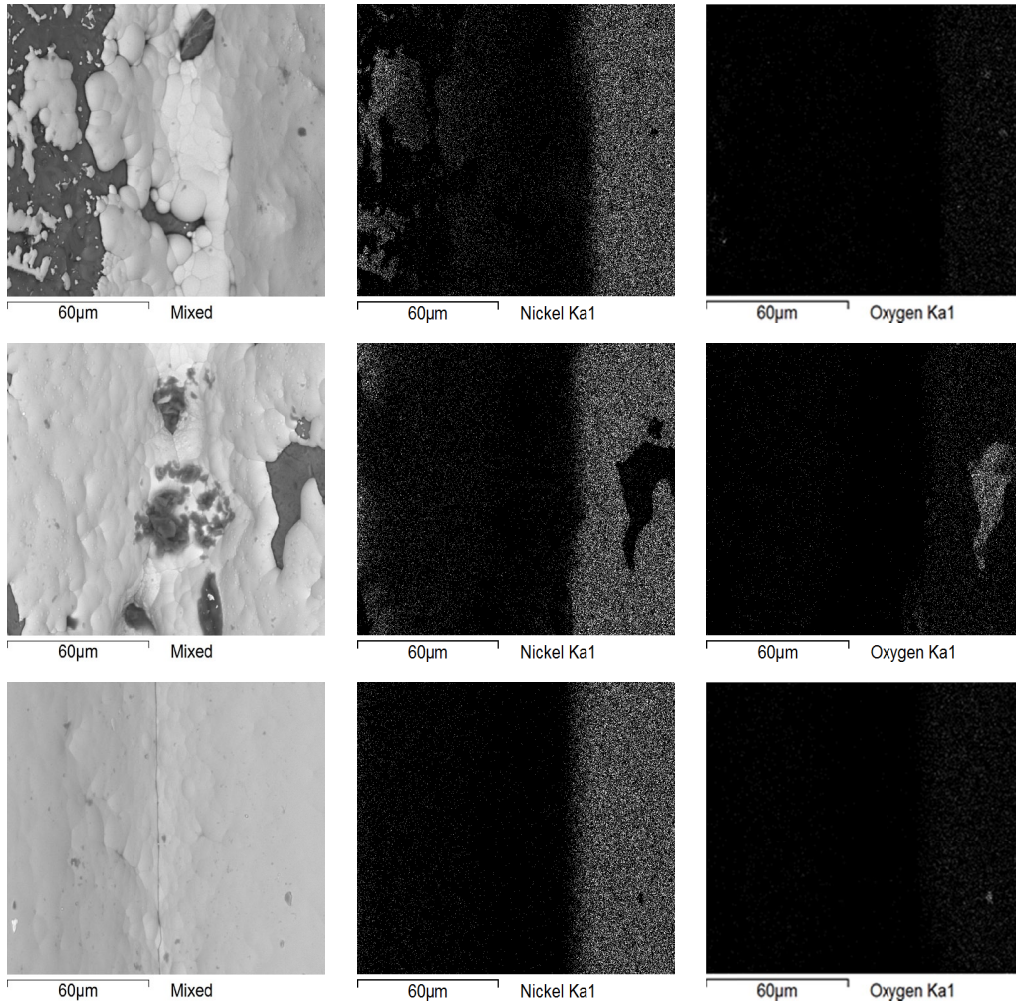


Fig. 10. EDS maps of the distribution of elements in nickel-coated samples' inner surfaces, for 10 min of nickel plating process and time of subcoating equalling: a) 1 min, b) 4 min, c) 5 min

coating of the inner part. In the exposed areas, not covered with nickel, apart from aluminum, oxygen was observed, which is characteristic of aluminum oxides.

In the case of the analysis of the effect of nickel time on the quality of nickel coatings, it was observed that by extending the nickel plating time, the layers deposited on inserts become more homogeneous, mainly in terms of inequalities visible in the SEM pictures.

In Fig. 11 the linear analysis of sample for reference parameters is presented, where 5 min of subcoating and 10 min

of actual nickel plating were applied. The presented graphs show a clear zoning, within which three zones can be distinguished: the sample core (from 0 to 60 µm), the transition zone (on the 60 to 70 µm section), and the outer layer constituting the proper nickel coating (within the range from 70 µm up to about 150 µm). In the sample core, signals from aluminum and silicone predominate, which is consistent with the composition of the alloy. There are also weaker oxygen signals. The nickel content in this section is very low. Only slight signals corresponding to this first grid may indicate impurities depos-

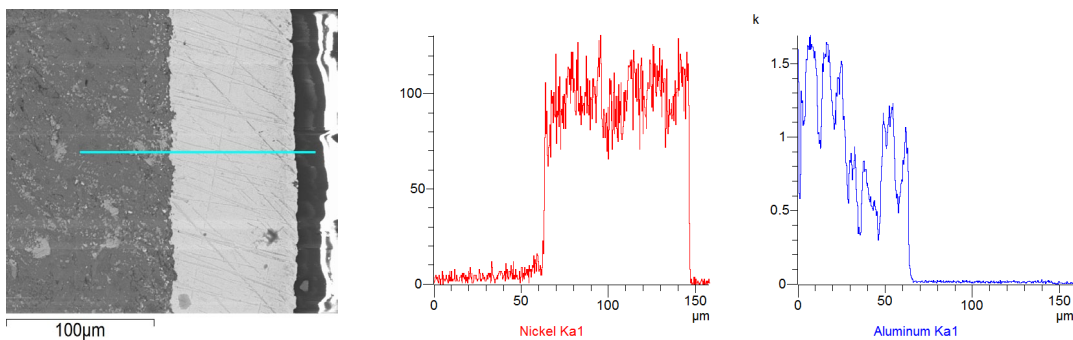


Fig. 11. EDS line scan along the blue line for sample nickel-plated for 10 min and subcoated for 5 min

ited during sample preparation (e.g. during polishing). In the transition zone, a sharp decrease in the aluminum content and an increase in the nickel content can be observed, as well as the peak for silicon and oxygen. This may prove the occurrence of oxidizing processes during the production of the nickel undercoating. Finally, in the outer layer, constituting the actual nickel coating, there are only signals from nickel and oxygen, and the intensity of signals from oxygen is at a similar level as in the sample core.

#### 4. Conclusions

The hereby proposed modified investment casting process, utilizing a 3D-printed polymer pattern, is an adequate technique for the flexible production of spatial castings to be used for the heat transfer enhancement in LTES units. Due to the selection of Al-Si alloy, the manufactured inserts are lightweight and complex in terms of shape, as this material possesses high flowability and therefore is a proper choice for the casting of thin-walled parts. In the first stage, the elaborated heat transfer enhancers were optimized regarding geometry, as several wall thicknesses and cell sizes were tested. The application of the fabricated castings in a one-insert test stand helped to reduce the time needed for the complete melting of the PCM deposit by 500-1000 s and decreased the temperature gradient between the bottom and the top zones of the accumulator by 2-3 times. The best outcomes were obtained for the type A insert, which was further applied in the second stage of investigation – a four-insert test stand (cell size of 23 mm, wall thickness of 1.2 mm, external global dimensions of 115 in diameter, and 180 in length). After a detailed analysis of the thermal performance of the up-scaled composite PCM heat accumulator, it can be concluded that, due to the e.g. natural convection, designed structures should differ on the height of the accumulator, so they could homogenize the temperature distribution more efficiently. In the lower zones of the PCM, the volume of inserts should be higher than in the upper ones. Moreover, to ensure corrosion protection during the long-term work of the evaluated cast structures in the molten salt environment, nickel-based galvanic coatings were considered. Nickel plating process parameters were adjusted, identifying the most promising plating and subcoating times as, respectively, 10 min and 5 min. The fabricated layers were characterized, confirming the formation of a homogeneous nickel coating.

#### Acknowledgments

This work has been developed in the frame of the ASTEP project, funded by the European Union's Horizon 2020 research program under grant agreement N°884411. Disclosure: The present publication reflects only the authors' views and the European Union is not liable for any use that may be made of the information contained therein.

#### REFERENCES

- [1] X. Dong, G. Gao, X. Zhao, Z. Qiu, C. Li, J. Zhang, P. Zheng, Investigation on heat transfer and phase transition in phase change material (PCM) balls and cold energy storage tank. *J. Energy Storage* **50**, 104695 (2022). DOI: <https://doi.org/10.1016/j.est.2022.104695>
- [2] T. Pirasaci, Investigation of phase state and heat storage form of the phase change material (PCM) layer integrated into the exterior walls of the residential-apartment during heating season. *Energy* **207**, 118176 (2020). DOI: <https://doi.org/10.1016/j.energy.2020.118176>
- [3] M.Y. Abdelsalam, P. Sarafraz, J.S. Cotton, M.F. Lightstone, Heat transfer characteristics of a hybrid thermal energy storage tank with phase change materials (PCMs) during indirect charging using isothermal coil heat exchanger. *Sol. Energy* **157**, 462-476 (2017). DOI: <https://doi.org/10.1016/j.solener.2017.08.043>
- [4] K.S. Dinesh, M. Chandrashekar, A systematic review of thermal energy storage and phase change materials. *NanoWorld. J.* **9**, S1, S364-S368 (2023). DOI: <https://doi.org/10.17756/nwj.2023-s1-071>
- [5] B. Anwar, M.A.A. Noon, H. Koten, Phase change materials (PCM) and their application. In: H. Koten (Ed.), *Recent researches in engineering sciences 2021*, Livre de Lyon (2021)
- [6] M.A.A. Noon, B. Anwar, H. Koten, Design and Fabrication of Solar Heat Cell Using Phase Change Materials. *Tech. J.* **26**, 1, 60-70 (2021), Retrieved from <https://tj.uettaxila.edu.pk/index.php/technical-journal/article/view/1508>
- [7] S. Zhang, D. Feng, L. Shi, L. Wang, Y. Jin, L. Tian, Z. Li, G. Wang, L. Zhao, Y. Yan, A review of phase change heat transfer in shape-stabilized phase change materials (ss-PCMs) based on porous supports for thermal energy storage. *Renew. Sust. Energ. Rev.* **135**, 110127 (2021). DOI: <https://doi.org/10.1016/j.rser.2020.110127>
- [8] X. Huang, C. Sun, Z. Chen, Y. Han, Experimental and numerical studies on melting process of phase change materials (PCMs) embedded in open-cells metal foams. *Int. J. Therm. Sci.* **170**, 107151 (2021). DOI: <https://doi.org/10.1016/j.ijthermalsci.2021.107151>
- [9] M. Aramesh, B. Shabani, Metal foam-phase change material composites for thermal energy storage: A review of performance parameters. *Renew. Sust. Energ. Rev.* **155**, 111919 (2022). DOI: <https://doi.org/10.1016/j.rser.2021.111919>
- [10] C.Y. Zhao, W. Lu, Y. Tian, Heat transfer enhancement for thermal energy storage using metal foams embedded within phase change materials (PCMs). *Sol. Energy* **84**, 8, 1402-1412 (2010). DOI: <https://doi.org/10.1016/j.solener.2010.04.022>
- [11] P. Zhang, X. Xiao, Z.W. Ma, A review of the composite phase change materials: Fabrication, characterization, mathematical modeling and application to performance enhancement. *Appl. Energ.* **165**, 472-510 (2016). DOI: <https://doi.org/10.1016/j.apenergy.2015.12.043>
- [12] Z. Wang, H. Zhang, B. Dou, G. Zhang, W. Wu, X. Zhou, Effect of copper metal foam proportion on heat transfer enhancement in the melting process of phase change materials. *Appl. Therm. Eng.* **201**, Part B, 117778 (2022). DOI: <https://doi.org/10.1016/j.applthermaleng.2021.117778>

- [13] K. Lafdi, M. Almajali, O. Huzayyin, Thermal properties of copper-coated carbon foams. *Carbon* **47**, 11, 2620-2626 (2009). DOI: <https://doi.org/10.1016/j.carbon.2009.05.014>
- [14] H. Schmit, C. Rathgeber, P. Hooek, S. Hiebler, Critical review on measured phase transition enthalpies of salt hydrates in the context of solid-liquid phase change materials. *Thermochim. Acta.* **683**, 178477 (2020). DOI: <https://doi.org/10.1016/j.tca.2019.178477>
- [15] Z. Li, Y. Lu, R. Huang, J. Chang, X. Yu, R. Jiang, X. Yu, A.P. Roskilly, Applications and technological challenges for heat recovery, storage and utilisation with latent thermal energy storage. *Appl. Energy* **283**, 116277 (2021). DOI: <https://doi.org/10.1016/j.apenergy.2020.116277>
- [16] U. Chadha, S.K. Selvaraj, H. Pant, A. Arora, D. Shukla, I. Sancheti, A. Chadha, D. Srivastava, M. Khanna, S.R. Kishore, V. Paramasivam, Phase change materials in metal casting processes: a critical review and future possibilities. *Adv. Mater. Sci. Eng.* **7520308** (2022). DOI: <https://doi.org/10.1155/2022/7520308>
- [17] B. Xu, P. Li, C. Chan, Application of phase change materials for thermal energy storage in concentrated solar thermal power plants: A review to recent developments. *Appl. Energy* **160**, 286-307 (2015). DOI: <https://doi.org/10.1016/j.apenergy.2015.09.016>
- [18] C. Vargel, Corrosion of Aluminium, 2004 Elsevier.
- [19] K. Labisz, L.A. Dobrzański, J. Konieczny, Anodization of cast aluminum alloys produced by different casting methods. *Arch. Foundry Eng.* **3**, 8, 45-50 (2008).
- [20] D. Kuang, L. Xu, L. Liu, W. Hu, Y. Wu, Graphene-nickel composites. *Appl. Surf. Sci.* **273**, 484-490 (2013). DOI: <https://doi.org/10.1016/j.apsusc.2013.02.066>
- [21] T. Oya, T. Nomura, M. Tsubota, N. Okinaka, T. Akiyama, Thermal conductivity enhancement of erythritol as PCM by using graphite and nickel particles. *Appl. Therm. Eng.* **61**, 825-828 (2013). DOI: <https://doi.org/10.1016/j.applthermaleng.2012.05.033>
- [22] T. Borkar, H. Mohseni, J. Hwang, T. W. Scharf, J.S. Tiley, S.H. Hong, R. Banerjee, Excellent strength-ductility combination in nickel-graphite nanoplatelet (GNP/Ni) nanocomposites. *J. Alloy. Compd.* **646**, 135-144 (2015). DOI: <https://doi.org/10.1016/j.jallcom.2015.06.013>
- [23] R.D. Rieke, Preparation of organometallic compounds from highly reactive metal powders. *Science* **246**, 4935, 1260-1264 (1989). DOI: <https://doi.org/10.1126/science.246.4935.1260>
- [24] O. Sadiku-Agboola, E.R. Sadiku, O.F. Biotidara, The properties and the effect of operating parameters on nickel plating (review). *Int. J. Phys. Sci.* **7**, 3, 349-360 (2012). DOI: <https://doi.org/10.5897/IJPS11.1163>
- [25] Q. Bao, W. Zheng, L. Chen, Z. Xu, J. Han, C. Zhu, Optimization of plating process and corrosion behavior of nanocrystalline Ni-Mo coatings on pure aluminum. *Colloid. Surface. A.* **636**, 128128 (2022). DOI: <https://doi.org/10.1016/j.colsurfa.2021.128128>
- [26] K.O. Cooke, P. Chudasama, Aluminium surface impregnated with nano constituents for enhanced mechanical performance. *Results. Phys.* **40**, 105826 (2022). DOI: <https://doi.org/10.1016/j.rinp.2022.105826>
- [27] A. Dmitruk, K. Naplocha, J. Grzęda, J. W. Kaczmar, Aluminum inserts for enhancing heat transfer in PCM accumulator. *Materials* **13**, 2, 415 (2020). DOI: <https://doi.org/10.3390/ma13020415>
- [28] W. Gai, W. Liu, Z. Deng, J. Zhou, Reaction of Al powder with water for hydrogen generation under ambient condition. *Int. J. Hydrogen. Energ.* **37**, 17, 13132-13140 (2012). DOI: <https://doi.org/10.1016/j.ijhydene.2012.04.025>
- [29] G. Kear, B.D. Barker, F.C. Walsh, Electrochemical corrosion of unalloyed copper in chloride media – a critical review. *Corros. Sci.* **46**, 1, 109-135 (2004). DOI: [https://doi.org/10.1016/S0010-938X\(02\)00257-3](https://doi.org/10.1016/S0010-938X(02)00257-3)
- [30] F. Clarelli, B. De Filippo, R. Natalini, Mathematical model of copper corrosion. *Appl. Math. Model.* **38**, 19-20, 4804-4816 (2014). DOI: <https://doi.org/10.1016/j.apm.2014.03.040>
- [31] D. Knotkova, K. Barton, Effects of acid deposition on corrosion of metals. *Atmos. Environ. A-Gen.* **26**, 17, 3169-3177 (1992). DOI: [https://doi.org/10.1016/0960-1686\(92\)90473-X](https://doi.org/10.1016/0960-1686(92)90473-X)
- [32] X.G. Zhang, Corrosion and Electrochemistry of Zinc, 1996 Springer Science+ Business Media, LLC, New York.
- [33] D.D.L. Chung, Review – Graphite. *J. Mater. Sci.* **37**, 1475-1489 (2002). DOI: <https://doi.org/10.1023/A:1014915307738>
- [34] R. Backreedy, J.M. Jones, M. Pourkashanian, A. Williams, A study of the reaction of oxygen with graphite: Model chemistry. *Faraday Discuss.* **119**, 385-394 (2001). DOI: <https://doi.org/10.1039/B102063N>
- [35] G. Mózes (Ed.), Paraffin Products, 1983 Elsevier.
- [36] T. Bauer, D. Laing, R. Tamme, Characterization of sodium nitrate as phase change material. *Int. J. Thermophys.* **33**, 91-104 (2012). DOI: <https://doi.org/10.1007/s10765-011-1113-9>
- [37] B.D. Iverson, S.T. Broome, A.M. Kruijenga, J.G. Cordaro, Thermal and mechanical properties of nitrate thermal storage salts in the solid-phase. *Sol. Energy* **86**, 10, 2897-2911 (2012). DOI: <https://doi.org/10.1016/j.solener.2012.03.011>
- [38] K. Vignarooban, X. Xu, A. Arvay, K. Hsu, A.M. Kannan, Heat transfer fluids for concentrating solar power systems – A review. *Appl. Energy.* **146**, 383-396 (2015). DOI: <https://doi.org/10.1016/j.apenergy.2015.01.125>
- [39] R.W. Bradshaw, R.W. Carling, A review of the chemical and physical properties of molten alkali nitrate salts and their effect on materials used for solar central receivers. *Proc. Vol.* **1987-7**, 959-969 (1987). DOI: <https://doi.org/10.1149/198707.0959PV>
- [40] Á.G. Fernández, L.F. Cabeza, Molten salt corrosion mechanisms of nitrate based thermal energy storage materials for concentrated solar power plants: A review. *Sol. Energ. Mat. Sol. C.* **194**, 160-165 (2019). DOI: <https://doi.org/10.1016/j.solmat.2019.02.012>
- [41] C.M. Kramer, Screening tests of sodium nitrate and potassium nitrate decomposition. *Sol. Energy* **29**, 5, 437-439 (1982). DOI: [https://doi.org/10.1016/0038-092X\(82\)90082-2](https://doi.org/10.1016/0038-092X(82)90082-2)
- [42] Z. Khan, Z. Khan, A. Ghafoor, A review of performance enhancement of PCM based latent heat storage system within the context of materials, thermal stability and compatibility. *Energy Convers. Manag.* **115**, 132-158 (2016). DOI: <https://doi.org/10.1016/j.enconman.2016.02.045>